Influence of Mechanical Properties on Milling of Amorphous and Crystalline Silica-Based Solids

Siwarote Siriluck[a], Umair Zafar[a], Colin Hare[a,1], Ali Hassanpour[a], Nadja T. Lönnroth[b,2], Navin Venugopal[b], Martin J. Murtagh[b,3], Mojtaba Ghadiri[a]

[a]*School of Chemical and Process Engineering, University of Leeds, LS2 9JT, UK*

[b]*Corning Incorporated, Corning, NY, United States*

*Corresponding Author: m.ghadiri@leeds.ac.uk

Abstract

Milling is an important and energy-intensive operation for preparing particulate solids to required specifications. It has been studied extensively to improve the rate of milling, energy utilisation and control of milling operations. With development of new materials and application of new milling systems, understanding the underlying science of milling is highly desirable for efficient and predictable size reduction. In the glass industry, silicate glasses have been developed with very special attributes, but the size reduction still poses many challenges. In this work, breakability and grindability of silicate materials in both crystalline and amorphous forms are investigated and correlations for their milling rate and energy utilisation as a function of material properties are developed. This involves physical and mechanical characterisation of the selected materials along with the analysis of milling rate in a single ball mill to develop a better understanding of the milling process. The breakability index, as described by the ratio of hardness to the square of toughness, describes well the milling rate of the crystalline form undergoing semi-brittle failure. The amorphous form of the test materials does not show a strong dependence on the breakability index, as the failure mode is brittle and dominated by pre-existing flaws.

---

[1] Current address: Chemical and Process Engineering, University of Surrey, Guildford, Surrey, GU2 7XH, UK
[2] Current Address: Helsinki R&D Center, Huawei Technologies Finland Oy Co. Ltd, Helsinki, Finland
3 Current Address: Materials Science and Engineering, Cornell University, ITHACA, NY, 14853-1501, USA

1. Introduction

Milling is an important unit operation in many industrial sectors such as mining and mineral, chemical, recycling and glass industry. This research work addresses the size reduction of silicates. These materials have special properties which have been explored by many manufacturing industries (Hao *et al.*, 2005; Boudrias *et al.*, 2001; Grujicic *et al.*, 2012). However, evaluation of milling technology and method for newly developed glasses is challenging due to their high hardness, toughness and stiffness, which require considerable energy to reduce their size. Therefore, it is of great interest to establish the most efficient size reduction method for both amorphous and crystalline structures of such materials.

Solids subjected to high mechanical stresses, exceeding a critical level, can develop micro-cracks. Yang and Hikosaka (1996), James *et al.* (2002), and Chadegnani *et al.* (2015) studied the propagation of cracks through glasses due to mechanical stressing. It was reported that the crack length is affected by the structure and existence of impurities. Chaudhri (2015) observed ring cracks on glass surfaces upon impact by a blunt indenter, causing elastic deformation followed by crack propagation. Ghadiri and Zhang (2002) analysed the chipping due to sub-surface lateral crack propagation for semi-brittle failure mode and proposed a model accounting for the mechanical properties. Shimamoto *et al.* (2016) described the dissipated energy in the fracture process and deduced a dimensionless group describing the propensity of chipping.

The milling process for glass materials has been studied extensively with the aim of improving the rate of milling, energy utilization and control of the milling process (see e.g. Fuerstenau and Abouzeid, 2002; Dovorak *et al*., 2016). These milling characteristics have been linked with the material physical and mechanical properties by Förch *et al*., 2009; Chen *et al*.,2010;, Gross and Tomozawa, 2008; Kjeldsen *et al*., 2013.

A large number of research works have been carried out on size reduction related to glass manufacturing over last few decades. Nevertheless, the ability to predict the milling performance of new and specialty glasses, such as lithium silicate and sodium aluminium silicate, is still limited, due to the complex nature of these materials. Therefore, in this work an attempt is made to understand the underlying science of milling for these materials, and to correlate the milling rate and energy utilisation to the physical and mechanical properties as proposed by Ghadiri and Zhang (2002).

2.   Material

Three sets of model material in two forms, amorphous and crystalline, were chosen and assessed for their milling. Fused silica and quartzite constituted one set and pairs of lithium silicate and sodium aluminium silicate (prepared in amorphous and crystalline forms) were the other two sets. All samples were cut into 7.5 mm edge cubes and supplied by Corning Inc., USA. Fused silica was obtained by melting and fast cooling of quartz sand. The crystalline quartzite was obtained from natural stones from Squaw Peak on Monument Mountain located in Great Barrington, Massachusetts, U.S.A. The silicate samples were produced at different cooling rates in order to create the amorphous and crystalline structures. The list of these model materials and their compositions are given in Table 1.

Table 1: List of model materials used in the milling investigation.

3.   Characterisation

The test materials were characterised for their physical and mechanical properties relevant to the size reduction as following.

3.1. X-Ray diffraction

The crystallinity of the crystalline samples was checked by X-ray diffraction using Phillips X-pert XRD equipment. Characteristics such as crystal structure and crystallite size have been determined. Quartzite has hexagonal structure, whilst crystalline lithium silicate and sodium aluminium silicate have orthorhombic structure (Glover and Ball, 1979). However, a comparison of the crystal lattices shows a longer and thus weaker bond in sodium aluminium silicate than lithium silicate sample (Tashiro *et al*., 1996; Boudrias *et al*., 2001). Scherrer's equation (Monshi *et al.,* 2012) is used to determine crystallite size, *L,* by diffraction angle XRD peaks. The data calculated for the three crystal samples are given in Table 2. The result shows that sodium aluminium silicate has the largest crystallite size, whilst lithium silicate has the smallest.

Table 2: Statistical data of crystallite sizes of silicate materials determined by Scherrer's equation along with crystal system from XRD.

3.2. Grain size

The average grain size was determined by SEM images using the Feret diameter method (Feret, 1930). The images were analysed by Image J software, and are shown in Figure 1. The

crystalline grains of quartzite, lithium silicate and sodium aluminium silicate have average sizes of 153, 282 and 186 µm, respectively, as measured over 50 grains.

Figure 1: The Ferret's diameter measurement from SEM images: (a) quartzite, (b) lithium silicate and (c) sodium aluminium silicate.

Overall from the structural characterisation, a clear difference is noted between all the model materials in terms of bond lengths, crystal structure, and crystallite and grain size. These are expected to influence the milling characteristics as it will be addressed below.

3.3. Density

Impact milling is influenced by particle density. Therefore the density of the supplied cubes of each material was measured using GeoPyc (Micromeritics, UK) and is given in Table 3 along with observations made using microscopy. Quartzite has the greatest density (2780 kg/m^3) whilst fused silica has the lowest (2190 kg/m^3). Based on the optical microscope observations, all the amorphous samples are transparent, whilst all the three crystalline samples are opaque.

Table 3: Density of all the six samples along with microscopic observations

3.4. Water vapour adsorption (DVS)

Environment relative humidity and temperature could influence the milling characteristics if the milled powder is hygroscopic. Water vapour adsorption of the silicate samples was investigated using dynamic vapour sorption (DVS) at different relative humidity values. The isotherm plots for the samples are shown in Figure A-1. Higher mass changes are observed for

5

the amorphous materials, e.g. sodium aluminium silicate sample has around 8.14 % change, whilst lower values are recorded for the crystalline materials; lithium silicate has around 0.4 % change.

3.5. Hardness and Young's modulus

Mechanical properties of silicate materials relevant to milling, i.e. hardness, elastic modulus and fracture toughness, were determined using both micro and nano-indentation techniques. Ball and Vickers indenters were used for the former and a Berkovich indenter for the latter. The NanoTest instrument manufactured by Micro Materials Ltd, Wrexham, UK, was used for nano-indentation. This provides a measure of force and penetration depth, from which the hardness, H, is inferred. The hardness of a material is defined by

$$H = \frac{F}{A} \tag{3.1}$$

where F is the maximum applied force and A is the plastic contact area. The contact area, A, is calculated from the penetration depth, h_c. The contact area for a Berkovich indenter, which has been used in this work, is given by Fischer-Cripps (2011) as:

$$Berkovich\ area = \sqrt[3]{3h_c}\ tan^2\ 65.3^o \tag{3.2}$$

Young's modulus of the specimen can be determined from the reduced modulus, E_r, of the contact and Poisson's ratio of the sample and indenter, as given by Fischer-Cripps (2011) as;

$$\frac{1}{E_r} = \frac{\left(1 - v_{sample}^2\right)}{E_{sample}} + \frac{\left(1 - v_{sample}^2\right)}{E_{indenter}} \tag{3.3}$$

where E and v are Young's modulus and Poisson's ratio, respectively. The hardness and Young's modulus of all the test materials were measured at different loads from 100 to at least 300 mN and different indentation positions on polished surfaces. The indents were inspected

by microscopy and those deemed reliable with good indent shape and far from grain boundaries were used for analysis. For determination of *H* and *E,* the loading-unloading curves for amorphous and crystalline silicate samples are shown in Figures 2 and 3, respectively.

Figure 2: The nano-indentation loading-unloading curves on fused silica (left), amorphous lithium silicate (middle) and amorphous sodium aluminium silicate (right). For illustrative purposes the starting displacements of the amorphous lithium and sodium alumina silicate are shifted to the right by 1.5 and 2.5 μm, respectively.

Figure 3: The nano-indentation loading-unloading curves on quartzite (left), crystalline lithium silicate (middle) and crystalline sodium aluminium silicate (right). For illustrative purposes the starting displacements of the lithium and sodium alumina silicates are shifted to the right by 1 and 2 μm, respectively.

The results show that the highest hardness is exhibited by the lithium silicate sample (around 8.5 GPa), whilst the lowest belongs to the crystalline sodium aluminium silicate (around 5.5 GPa). However, in the case of Young's modulus results, fused silica has the highest value of around 83.2 GPa and lithium silicate has the lowest value of around 66.3 GPa. Hardness and reduced modulus results are summarized in Table 4. Nevertheless, the range of hardness and Young's modulus values for all the test materials is narrow. It is noteworthy that the above analysis describes the hardness and Young's modulus of individual crystallites within the specimen cube, as nano-indention has a very small footprint. The mechanical properties of the

cubes of crystalline structures would be different as they are made up of multiple crystallites, adhering together. In order to obtain the relevant properties in the latter case, the indentation footprint should be much larger than the crystallite size. For this reason, micro-indentation was also carried out with a spherical ball indenter (stainless steel A420) using an Instron 5566 mechanical tester according to Lawn (1998). The projected area is calculated here from the measured penetration depth (h_c) by

$$A_{projected\ circle\ area} = \pi \left(d_b h_c - h_c^2 \right) \tag{3.4}$$

The measurements here at large scales are referred to as 'Bulk'. It can be seen from Table 4 that the 'Bulk' values of H and E are much lower than those obtained by nano-indentation on the same test specimens.

3.6. Fracture toughness

The fracture toughness of the test materials was also determined at the two size scales: one at small scale on individual crystallites forming the test specimens, and another at large scale on the actual test specimens, referred to as bulk scale. For the former, indentation fractures were made on individual crystallites and Laugier's equation (1985) was used to calculate the indentation fracture toughness:

$$K_{lc} = 0.010 \left(\frac{E}{H} \right)^{\frac{2}{3}} \left(\frac{F}{C^{\frac{3}{2}}} \right) \tag{3.5}$$

where H and E are hardness and Young's modulus, respectively. For tests on single crystallites, the values of hardness and Young's modulus as given by Berkovich indenter were used in the calculation of K_{lc}. C is the crack length from the centre of the indent to the tip of the crack and F is the applied load. For amorphous specimens cracks were made by a Vickers indenter, whilst for tests on individual crystallite grains this was done by a Berkovich indenter.

Several positions were tested with the load range 0.75 – 2 N. An example of indentation at 1.5 N load by micro indentation is presented in Figure 4, where the crack length was measured from SEM images using Image J software. The average values of fracture toughness are shown for all materials in Table 4. The calculated results show that fused silica has the highest fracture toughness, with a value around 1.9 MPa.m$^{0.5}$, whilst amorphous lithium silicate and crystalline sodium aluminium silicate have the lowest (around 0.6 MPa.m$^{0.5}$).

Figure 4: Vickers indent at 1.5 N load on sodium aluminium silicate with diagram of the half length of the diagonal indent (a) and diagram of crack length (b).

Fracture toughness was also measured at bulk scale using large specimens because the crystalline samples were made of small crystallite grains and crack initiation and propagation initially proceeded through grain boundaries. Therefore, the inter-grain fracture toughness was measured using the single edge notched beam test based on the procedure by Nose and Fujii (1988). In this test, a notch was cut in the middle of each sample and the crack length of notch (C_n) was measured and fracture toughness is calculated using Eq. 3.7.

$$K_{1C} = \frac{PS_w}{BW^{3/2}} \left[2.9\left(\frac{c_n}{W}\right)^{\frac{1}{2}} - 4.60\left(\frac{c_n}{W}\right)^{\frac{3}{2}} + 21.8\left(\frac{c_n}{W}\right)^{\frac{5}{2}} - 37.6\left(\frac{c_n}{W}\right)^{\frac{7}{2}} + 38.7\left(\frac{c_n}{W}\right)^{\frac{9}{2}} \right]$$

(3.7)

where span width (S_w), width (W) and base (B) dimensions used were 7.5, 3.3 and 3.2 mm, respectively.

Measuring the fracture toughness in this way, it was found that crystalline sodium aluminium silicate has the lowest inter-grain fracture toughness (around 0.5 MPa.m$^{0.5}$). Using the data of hardness and fracture toughness, the breakability index (H/K_c^2), as defined by the model of Ghadiri and Zhang (2002), was calculated for all the test materials and is shown in Table 4. The breakability index is highest for amorphous lithium silicate and lowest for crystalline lithium silicate. It is noteworthy that the breakability index is different by considering whether the crack propagation occurs at grain boundaries or through the crystallites.

Table 4: Mechanical properties of the test materials obtained by nano-indentations on single crystallites and by micro-indentation on bulk crystalline cubes, and their breakability index.

4.   Milling Results and Discussion

The milling of the six silicate materials was carried out using a Retsch MM200 single ball mill and the milling behaviour and breakage mechanism in terms of fracture, micro cracks, chipping and fragmentation were analysed. The milling setup is shown in Figure 5, which consists of a stainless steel grinding capsule with a central cylindrical section of length 38.8 mm and radius 9 mm, and two hemi-spherical ends of the same radius, giving an internal volume of 11 ml. A 12 mm stainless steel ball is used as grinding medium and placed inside the chamber along with one cube of the sample. The chamber is then oscillated horizontally along an arc with an amplitude of 8.9 mm and a frequency of 30 Hz. Each 7.5 mm cube of the six silicate samples was milled individually and each test repeated three times. First, the milling process of a quartzite cube in a Perspex capsule was recorded using high speed video recording at 500 frames per second (fps). Multiple movement patterns of the grinding medium and the sample

cube were observed in the grinding chamber, which included static, short swirling, vertical motion, long swirling, rolling and impacting and fly impacting. These patterns are shown in Figure 6. For static and short swirling patterns at the start of the process, no size reduction was observed.

Figure 5: Milling equipment: (a) the Retsch MM 200 single ball mill (b) the stainless steel grinding capsule.

Figure 6: Movement of 12 mm grinding media and cube sample at 30 Hz; (a) static pattern; (b) short swirling; (c) vertical movement; (d) long swirling; (e) roll impacting; (f) fly impacting.

The particle size distribution was measured by laser light diffraction using Malvern Mastersizer 2000 and also viewed by SEM. Furthermore, the applicability of a first order milling rate, as described by Kwan *et al.*, (2003), was explored and its rate constant was calculated by Eq. 3.8.

$$\frac{D_t - D_o}{D_o - D_l} = exp(-K_p t)$$

(3.8)

where, D_t is the D_{50} of the particles at grinding time (t), D_o is the D_{50} of the particles at original time and D_l is the D_{50} of the grinding limit of the particles, as determined by the test case in which no further size reduction takes place as milling is continued. K_p is the first order milling rate constant of the material. The influence of relative humidity on the milling rate constant was assessed by conditioning the sample at four different relative humidity values of 5, 11, 44 and 74% RH using saturated salt solutions. The results are shown in Figure 7, where the normalised particle size (D_{50}) is given as a function of time. A first order rate process fits nicely

for the cases of amorphous materials (a), (b), (c), whilst a two-stage rate process is observed for the crystalline materials with two different rate constants. Initially the crystallites break off from the cube and then they undergo breakage at a later stage. The fitting is poor for case (f) because sodium aluminium silicate sticks to the mill walls making the determination of the rate constant inaccurate.

Using the measured data (consisting of the grinding size limit, D_{50} of the particles at a given grinding time and the D_{50} of the feed particles) a first order milling rate was fitted using the Generalised Reduced Gradient algorithm (GRG). The average rate constant (K_p) was determined for all the silicate materials and for the four relative humidity values. Clearly, the relative humidity has little effect on the milling rate and grinding size limit as shown in Figure 7. Average K_p for each material type was determined from the GRG fits, by taking average K_p over all humidities; these are given in Table 5. However for relating the milling rate to the mechanical properties, the value of K_p at 44% RH is used, as hardness and toughness were measured in room normal condition at nearly the same RH. This is also given in Table 5. The crystalline materials have two K_p's due to change in breakage behaviour, the material first is broken into single crystallites, followed by the milling of them. The breakage mechanism was qualitatively assessed by the inspection of SEM images shown in Figures A2-A7. For amorphous silicate materials, it was observed that the breakage process during the initial stages of milling is by the chipping mechanism through concoidal fracture at the edges and corners. Once these surfaces undergo fatigue, rapid fragmentation and disintegration by fracture takes place. The fragments then further break down, producing fine particles and eventually reaching the grinding limit size. However, for the crystalline materials, the chipping stage is followed by disintegration into single crystallite grains, i.e. grain boundary fracture takes place, and the grains are then milled to the grinding limit size. A slightly different scenario prevails for

12

crystalline lithium silicate. It was observed that after chipping, the fines produced adhered strongly to the mother cube in a thin surface coating and acted as a cushion slowing down further milling.

Table 5 K_P for all materials as determined from GRG fits to the size reduction data, average value over all humidities and the value at 40% RH as used in the calculations.

Furthermore, the extent of breakage as a function of grinding time was quantitatively analysed for all the test materials using the particle size distributions obtained from Malvern Mastersizer 2000. There are a number of PSD models such as Guadin-Shuhmann, Gamma function, Gumbel, normal distribution and Rosin-Rammler (Allen *et al*. 2016, Merkus 2016). However, in this work, the Rosin-Rammler model, which is based on $D_{63.2}$ of the particle size distribution, provides the best fit for all the particle size distributions as shown in Figure 8. It was found that the grinding size limit for most of the materials was reached in a short grinding time of around 180 s, as the PSD approached a final one at long times, although the distributions in Figure 8 a, c and d have still some way to get to the limit value. The PSD for the crystalline lithium silicate differs in its temporal evolution (see Figure 8 (e)). This is because as the fine particles are formed they stick to the mother cube, so the PSD is essentially that of fine particles, which remains unchanged, so the PSD of long times is shown.

Figure 7: Size reduction ratio of amorphous (a-c) and crystalline specimens (d-f) as a function of grinding time at 30 Hz for each six materials at 4 different relative humidities from 5 to 74%RH; (a) fused silica; (b) lithium silicate; (c) sodium aluminium silicate; (d) quartzite; (e) lithium silicate; (f) sodium aluminium silicate.

Figure 8: The fitted cumulative Rosin-Rammler distribution model compared with the experimental data of amorphous (a-c) and crystalline specimens (d-f) for various grinding times for; (a) fused silica; (b) lithium silicate; (c) sodium aluminium silicate; (d) quartzite; (e) lithium silicate; (f) sodium aluminium silicate.

(c)

In milling processes, the energy utilisation is considered as the most important parameter for assessing efficiency. It depends on a large number of parameters, such as feed particle properties and process variables, such as the dynamics of the mill (stressing frequency and magnitude) and the way energy is expended in size reduction. The energy utilisation is obtained from the ratio of the specific new surface area (ΔSSA) obtained from PSD (as calculated from the particle size analysis based on laser light diffraction measurements, given by Malvern Mastersizer 2000) divided by specific energy consumption (E_c). In this work, the latter is estimated using numerical simulations by the Discrete Element Method (DEM), where the dynamics of particle motion in the mill is analysed and the dissipated collisional energy of the particles is calculated. In the DEM simulations the geometry and its motion are replicated exactly as in the experimental device, the milling ball is represented as a single sphere, whilst the cube sample is represented by the clumped sphere method (Favier *et al.*, 2001) to approximate the cubic shape. The 7.5 mm cube is approximated using spheres of 2.5 mm radius, with the distance between centres of neighbouring spheres being equal to half the radius (1.125 mm), therefore three spheres are required along each edge, resulting in a total of 27 spheres. The Hertz-Mindlin contact model is used, with input parameters taken from literature reported by Zok *et al. (*2004), Aboushelib *et al. (*2005), Sivamani *et al. (*2003), Knight *et al. (*1977) Frechette (2012) and this work (given in Table A-2). It should be noted that bulk value of Young's modulus as given in Table 4 is used here. The media ball and the sample are generated inside the mill geometry and allowed to settle under gravity until they come to rest (0.2 s) before the mill motion is initiated and maintained for a period of 10 s. All collisions between the sample and the media ball and vessel walls are analysed and the energy of each collision, E_{coll}, is given by Eq. 3.9:

$$E_{coll} = \frac{1}{2} M^* V_R^2 \qquad\qquad (3.9)$$

where V_R is the relative velocity between the two colliding elements and M^* is the reduced mass, given by:

$$M^* = \frac{M_s \cdot M_e}{M_s + M_e}$$

where M_s is the mass of the sample and M_e is the mass of the other colliding element. For collisions with the vessel wall the mass was considered to be infinite, resulting in the reduced mass being equal to that of the sample. The total energy arising from all collisions during the 10 s of shaking was considered. Simulations were carried out for cubic samples representing fused silica and quartzite. The dissipated energy depends on Young's modulus, density and dissipative processes and these are taken into account in DEM simulations. The results showed that the majority of the dissipated energy (69.2 % and 72.8 % for fused silica and quartzite, respectively) is due to collisions with the hemispherical ends of the grinding capsule, and 27.7 and 23.1 % is due to collisions with the grinding ball, with the remainder attributed to collisions with the cylindrical section of the vessel. The simulations estimated the dissipated power to be 1.89 W for both fused silica and quartzite samples. These data were then used along with the experimentally measured particle size distributions to calculate the energy utilisation for different grinding times. The ratio of change in the specific surface area, as calculated by Malvern Mastersizer 2000, and the specific energy consumption due to collisions, as determined from DEM simulations, were then used in the calculation of the energy utilisation. The results are shown in Figure 9. Clearly the energy utilisation of fused silica is much larger than that of quartzite. It appears that the energy utilisation of fused silica goes through a peak, suggesting there exist an optimum time for maximum change in the surface area.

Figure 9: Energy utilisation of fused silica and quartzite as a function of grinding time.

As described previously, the milling rate constant shows a strong correlation with the breakability index for crystalline materials. Two distinct stages of size reduction are observed, corresponding to initial chipping and then fragmentation by grain boundary fracture (inter-crystallite) followed by crystallite breakage. Here, the relevant H and K_c, as given in Table 4, together with K_p values from Table 5 are used as appropriate.

For the amorphous structures, chipping takes place first by concoidal cracks, followed by the propagation of micro-cracks developed on the edges and corners, leading to fragmentation and eventually milling of the fragments to the size limit. The breakability index varies considerably from about 2 to 40 m^2/J, while the milling rate constant varies in a very narrow range of 0.18 to 0.21 s^{-1} for all three materials (Figure 10). Thus, the milling rate is fast, but is nearly independent of the breakability index. This is expected as the failure mode of the amorphous version of the test materials is essentially brittle and dependent on flaws that are present or develop during the initial stages of mechanical stressing. For the crystalline materials strong correlations are observed between the breakability index and milling rate in line with the previous work on single organic crystals (Ghadiri *et al.*, 2007; Kwan *et al.*, 2005). This is the case here for both inter-crystallite failure along grain boundaries (Figure 11) and crystallite fracture (Figure 12). In the crystalline materials plots (Figures 11 and 12) it should be remembered that the lithium silicate ($Li_2Si_2O_5$) powder sticks to the mother cube and therefore it is difficult to distinguish between crystallite breakage and inter-crystallite boundary fracture. It is noteworthy that K_c values for both cases are nearly the same as given in Table 4. K_p values are also similar. Based on the SEM observations, cracks propagate through both crystallites and inter-crystallite boundaries, as shown in Figure 13. The milling process in this case is therefore by combined fracture of crystallites, and inter-crystallite grain boundary failure, rather than the latter alone, and therefore the following data are used: K_p= 0.013 1/s, H/K_c^2 =

1.11 m^2/J (H=1.15 GPa, K_c=1.02 MPa.m$^{0.5}$). So for all crystalline materials tested here the milling rate is correlated with the breakage index for both initial inter-crystallite breakage at grain boundaries and final crystallite fracture.

For the amorphous materials the case is different as no clear correlation was observed. This could be related to the brittle failure, as evidenced by the presence of concoidal fracture, as the breakability index is not descriptive of the process, whilst for the crystalline materials the good correlations suggest the breakage is by semi-brittle failure mode involving dislocation pile-up for crack initiation.

It is also noteworthy that the breakability index is based on the quasi-static characterisation of hardness and toughness. This suggests that these properties are not sensitive to strain rate for the crystalline materials analysed in this work. In contrast, for the case of organic solids previously studied (Kwan *et al.*, 2005), the hardness and toughness were indirectly inferred by impact testing, as they were dependent on strain rate.

Figure 10: The milling rate constant as a function of breakability index for amorphous silicate materials.

Figure 11: Milling rate constant for bulk crystalline specimens, representing inter-crystallite fracture along grain boundaries as a function of the breakability index for crystalline silicate materials.

Figure 12: Milling rate constant for crystallite milling as a function of breakability index.

Figure 13 SEM micrographs of lithium silicate showing the crystallite and a crack generated from outside the crystallite and going through it and out again.

Conclusions

In this work, a set of three silicate materials in two forms, amorphous and crystalline, were chosen to assess differences in their milling behaviour. The milling performance was assessed on single cubes of each test material using a single ball mill at different relative humidity values. It was found that relative humidity had no notable influence on the milling rate. The amorphous form of the test materials underwent chipping by conchoidal fracture initially, followed by propagation of cracks into the body of the specimens. In contrast, the crystalline forms initially failed by crystallite grain boundary failure, followed by the fracture of the crystallite grains. A first order milling rate described the size reduction of the amorphous forms, whilst the crystallite forms showed a more complex breakage rate, which was approximated by two sequential first order rate processes. For both amorphous and crystalline forms, sodium aluminium silicate has the largest milling rate constant, albeit by different mechanisms for crack initiation and propagation.

The breakability index as described by H/K_c^2 was used to explore the dependence of the milling rate constant on the mechanical properties. As intuitively expected, the amorphous form of the test materials does not show a strong dependence on H/K_c^2, as the failure mode is brittle, for which pre-existing flaws are responsible for crack propagation. In contrast, the crystalline forms show strong correlations for both inter-crystallite grain boundary failure as well as crystallite milling, implicitly suggesting that they both undergo semi-brittle failure. In this case, the milling rate constant increases with the breakability index. The breakability index H/K_c^2 describes the milling rate consistently for all the three materials structures, i.e.

19

amorphous, inter-crystallite grain and crystallite, separately. However, considering each material on its own, the trend is different for the amorphous and crystallite forms. For example for sodium aluminium silicate the value of H/K_c^2 is nearly the same for both amorphous and inter-crystallite grain structures (around 4.3 m^2/kJ), but the milling rate constant of the amorphous form is about half of that of the inter-crystallite form. Similarly the crystallite form of the same material has a large value for H/K_c^2, as compared to that of inter-crystallite form, but its milling rate constant is roughly a third of the latter form. A similar trend is also seen for fused silica (amorphous) and lithium silicate (crystalline). A summary of the characterisation results is shown in Table 6. In conclusion, within each set of structures (i.e. amorphous or crystalline) the milling rate constant is described by the breakability index. However, not surprisingly, the breakability index does not account for changes in the intermolecular structure as the silicates transform from amorphous to crystalline, and for the differences in the bulk ensemble of bonded crystallites and individual crystallites.

Table 6 Summary of mechanical and milling characterisation.

Acknowledgements

References

Aboushelib, M. N., N. De Jager, C. J. Kleverlaan and A. J. Feilzer. 2005. Microtensile bond strength of different components of core veneered all-ceramic restorations. *Dental Materials,* 21(10), pp.984-991.

Allen, P. A., N. A. Michael, M. D'arcy, D. C. Roda-Boluda, A. C. Whittaker, R. A. Duller and J. J. Armitage. 2016. Fractionation of grain size in terrestrial sediment routing systems. *Basin Research*.

Boudrias, P., S. Sakkal and Y. Petrova. 2001. Anatomical post design meets quartz fiber technology: rationale and case report. *Compendium of continuing education in dentistry (Jamesburg, NJ: 1995),* 22(4), pp.337-40, 342, PMID: 11913279. https://pubmed.ncbi.nlm.nih.gov/11913279/

Chadegani, A., Iyer, K.A., Mehoke, D.S. and Batra, R.C. 2015. Hypervelocity impact of a steel microsphere on fused silica sheets. International Journal of Impact Engineering. 80, pp.116-132.

Chaudhri, M. M. 2015. Dynamic fracture of inorganic glasses by hard spherical and conical projectiles. *Phil. Trans. R. Soc. A,* 373(2038), pp.2014-2035.

Chen, X., M. A. Rickard, J. W. Hull Jr, C. Zheng, A. Leugers and P. Simoncic. 2010. Raman spectroscopic investigation of tetraethylammonium polybromides. *Inorganic chemistry,* 49(19), pp.8684-8689.

Dutta, A.K. and D. Penumadu. 2007. Hardness and modulus of individual sand particles using nanoindentation. *Conference: Geo-Denver 2007.* DOI: 10.1061/40917(236)34.

Dvorak, K., Dolak, D. and Hajkova, I. 2016. Impact of Grinding Technology on Final Properties of Portland Cement. Key Engineering Materials. 677, 191-196.

Favier, J. F., M.H. Abbaspour-Fard, M. Kremmer, 2001. Modeling Nonspherical Particles Using Multisphere Discrete Elements, *Journal of Engineering Mechanics*, 127(10), pp.971-977.

Feret, L.R. 1930. La grosseur des grains des matières pulvérulentes, Premières Communications de la Nouvelle Association Internationale pour l'Essai des Matériaux, Groupe D, 1930, pp. 428–436.

Fischer-Cripps, A.C. 2011. *"Nanoindentation" Springer*, New York, pp. 5-7, New York, NY, ISBN 978-1-4614-2960-9

Förch, R., H. Schönherr, A. Tobias, A. Jenkins. 2009. *Surface design: Applications in bioscience and nanotechnology.* Wiley-VCH Verlag GmbH & Co. KGaA, DOI:10.1002/9783527628599.

Frechette, V. 2012. *Surfaces and interfaces of glass and ceramics.* Volume 7 of Materials Science Research, Springer Science & Business Media, ISBN 1468431447, 9781468431445.

Fuerstenau, D. and Abouzeid, A.-Z. 2002. The energy efficiency of ball milling in comminution. International Journal of Mineral Processing. 67(1), pp.161-185.

Ghadiri, M, Kwan, CC, Ding, YL, 2007. Analysis of Milling and the Role of Feed Properties. Particle Breakage, *Handbook of Powder Technology*. 12, Pages: 605-634.

Ghadiri, M. and Z. Zhang. 2002. Impact attrition of particulate solids. Part 1: a theoretical model of chipping. *Chemical Engineering Science,* 57(17), pp.3659-3669.

Glover, G. and Ball, A. 2014. THE DEFORMATION AND FRACTURE OF QUARTZ. In: Engineering Applications of Fracture Analysis: Proceedings of the First National Conference on Fracture Held in Johannesburg, South Africa, 7-9 November 1979: Elsevier, pp.419-428

Gross, T. and M. Tomozawa. 2008. Indentation-induced microhardness changes in glasses: Possible fictive temperature increase caused by plastic deformation. *Journal of Non-Crystalline Solids,* 354(34), pp.4056-4062.

Grujicic, M., W. Bell and B. Pandurangan. 2012. Design and material selection guidelines and strategies for transparent armor systems. *Materials & Design,* 34, pp.808-819.

Hao, L., H. Spoon, G. Sloan, J. Marshall, L. Armus, A. Tielens, B. Sargent, I. Van Bemmel, V. Charmandaris and D. Weedman. 2005. The detection of silicate emission from quasars at 10 and 18 microns. *The Astrophysical Journal Letters,* 625(2), pL75.

James, S.H., Nordby, J.J. and Bell, S. 2002. Forensic science: an introduction to scientific and investigative techniques. CRC Press, ISBN-0-8493-1246-9.

Kjeldsen, J., M. M. Smedskjaer, J. C. Mauro, R. E. Youngman, L. Huang and Y. Yue. 2013. Mixed alkaline earth effect in sodium aluminosilicate glasses. *Journal of Non-Crystalline Solids,* 369, pp.61-68.

Knight, C., M. V. Swain and M. Chaudhri. 1977. Impact of small steel spheres on glass surfaces. *Journal of Materials Science,* 12(8), pp.1573-1586.

Kwan, C. C., M. Ghadiri, D. G. Papadopoulos and A. C. Bentham. 2003. The effects of operating conditions on the milling of microcrystalline cellulose. *Chemical engineering & technology,* 26(2), pp.185-190.

Kwan, C. C., H. Mio, Y. Q. Chen, Y. L. Ding, F. Saito, D. G. Papadopoulos, A. C. Bentham and M. Ghadiri. 2005. Analysis of the milling rate of pharmaceutical powders using the Distinct Element Method (DEM). *Chemical engineering science,* 60(5), pp.1441-1448

Laugier, M. 1985. Toughness determination of some ceramic tool materials using the method of Hertzian indentation fracture. *Journal of materials science letters,* 4(12), pp.1542-1544.

Lawn, B. R. 1998. Indentation of ceramics with spheres: a century after Hertz. *Journal of the American Ceramic Society,* 81(8), pp.1977-1994.

Merkus, H. G. 2016. Introduction. *Production, Handling and Characterization of Particulate Materials.* Eds: H.G. Merkus and G.M.H. Meesters, Springer, pp.1-29. ISBN978-3-319-79323-8, DOI:https://doi.org/10.1007/978-3-319-20949-4.

Monshi, A., M. R. Foroughi and M. R. Monshi. 2012. Modified Scherrer equation to estimate more accurately nano-crystallite size using XRD. *World Journal of Nano Science and Engineering,* 2(03), pp.154-160.

Neuville, D. R., L. Cormier and D. Massiot. 2006. Al coordination and speciation in calcium aluminosilicate glasses: Effects of composition determined by 27 Al MQ-MAS NMR and Raman spectroscopy. *Chemical geology,* 229(1), pp.173-185.

Nose, T. and T. Fujii. 1988. Evaluation of Fracture Toughness for Ceramic Materials by a Single-Edge-Precracked-Beam Method. *Journal of the American Ceramic Society,* 71(5), pp.328-333.

Shimamoto, K., Y. Sekiguchi and C. Sato. 2016. The critical energy release rate of welded joints between fiber-reinforced thermoplastics and metals when thermal residual stress is considered. *The Journal of Adhesion,* 92(4), pp.306-318.

Sivamani, R. K., J. Goodman, N. V. Gitis and H. I. Maibach. 2003. Coefficient of friction: tribological studies in man–an overview. *Skin Research and Technology,* 9(3), pp.227-234.

Tashiro, K., Sasaki, S. and Kobayashi, M. 1996. Structural investigation of orthorhombic-to-hexagonal phase transition in polyethylene crystal: the experimental confirmation of the conformationally disordered structure by X-ray diffraction and infrared/Raman spectroscopic measurements. *Macromolecules.* **29**(23), pp.7460-7469.

Yang, G., Hikosaka. H. 1996. Crack length and specimen size influences on fracture strength of brittle materials. *Construction and Building Materials*, 10 (8), pp. 565-570.

Zok, F. W., S. A. Waltner, Z. Wei, H. J. Rathbun, R. M. Mcmeeking and A. G. Evans. 2004. A protocol for characterizing the structural performance of metallic sandwich panels: application to pyramidal truss cores. *International Journal of Solids and Structures,* 41(22), pp.6249-6271

Appendixes

Table A-1: XRD data of three crystalline materials.

Figure A-1: Contact angle measurement for (a) amorphous fused silica; (b) amorphous lithium silicate; (c) amorphous sodium aluminium silicate; (d) crystalline quartzite; (e) crystalline lithium silicate; (f) crystalline sodium aluminium silicate

Figure A-2: SEM images of milled fused silica; (a) breakage and fatigue on mother particle; (b) chipped particles from mother particles; (c) coarse particles; and (d) milled sample at 180 s

Figure A-3: SEM images of milled amorphous lithium silicate; (a) breakage on mother particles; (b) chipped particles from mother particles; (c) coarse particles; (d) milled sample at 180 s.

Figure A-4: SEM images of milled amorphous sodium aluminium; (a) breakage on mother particles; (b) chipped particles from mother particles; (c) coarse particles; (d) milled sample at 180 s.

Figure A-5: SEM images of crystalline quartzite; (a) corner and edge damage, at grinding time of 2 s; (b) chipped hexagonal quartzite grains; (c) the liberated quartz grains; and (d) grinding limit size of quartzite.

Figure A-6: SEM images of crystalline lithium silicate; (a) fresh origanl surface; (b) corner of mother particle after chipping at grinding time of 1 s; (c) and (d) the crushed mother particle surface.

Figure A-7: SEM images of crystalline sodium aluminium silicate; (a) corner of mother particle at 1 s; (b) chipped grain particle; (c) the liberated quartz grains; and (d) grinding limit size.

Table A-2: Materials parameters of materials used in the simulations.

Influence of Mechanical Properties on Milling of Amorphous and Crystalline Silica-Based Solids

Table 1: List of model materials used in the milling investigation.

Pair	Amorphous	Crystalline
1	Fused Silica SiO_2	Quartzite $\alpha\text{-}SiO_2$
2	Lithium silicate 33.3 Li_2O-66.6 SiO_2	Lithium silicate $Li_2Si_2O_5$
3	Sodium aluminium silicate 25 Na_2O-25 Al_2O_3-50 SiO_2	Sodium aluminium silicate $NaAl(SiO_4)$

Table 2: Statistical data of crystallite sizes of silicate materials determined by Scherrer's equation along with crystal system from XRD.

Type of Materials	Mean, (Å)	Max, (Å)	Min, (Å)	Crystalsystem
Quartzite	1240	1905	704	Hexagonal
Lithium silicate	598	1186	46	Orthorhombic
Sodium aluminium silicate	1655	31278	34	Orthorhombic

Table 3: Density of all the six samples along with microscopic observations.

Structure type	Materials	Density (kg/m³)	Microscope observation
Amorphous	Fused silica	2190 ± 0.85	Transparent, no bubbles
	Lithium silicate	2320 ± 1.60	Transparent, small bubbles
	Sodium aluminium silicate	2570 ± 0.56	Transparent, large bubbles
Crystalline	Quartzite	2780 ± 0.24	Opaque
	Lithium silicate	2520 ± 2.91	Opaque
	Sodium aluminium silicate	2450 ± 1.88	Opaque

Table 4: Mechanical properties of the test materials obtained by nano-indentations on single crystallites and by micro-indentation on bulk crystalline cubes, and their breakability index.

	Materials	H (GPa)	E (GPa)	K_c (MPa.m$^{0.5}$)	H/K_c^2 (m^2/kJ)
Amorphous	Fused Silica	6.7 ± 0.03	83.1 ± 0.03	1.91 ± 0.2	1.82
	Lithium silicate	8.6 ± 0.08	66.3 ± 0.06	0.64 ± 0.13	20.90
	Sodium aluminium silicate	7.2 ± 0.04	73.2 ± 0.05	1.3 ± 0.06	4.27
Crystalline	Quartzite	8.2 ± 0.09	78.0 ± 0.1	1.2 ± 0.06	6.06
	Lithium silicate	6.4 ± 0.04	69.2 ± 0.04	1.0 ± 0.04	5.94
	Sodium aluminium silicate	5.4 ± 0.05	71.3 ± 0.1	0.7 ± 0.07	9.93
	Quartzite (Bulk)	1.4 ± 0.3	12.7 ± 0.2	0.7 ± 0.02	2.88
	Lithium silicate (Bulk)	1.1 ± 0.4	10.6 ± 0.15	1.02 ± 0.1	1.11
	Sodium aluminium silicate (Bulk)	1.2 ± 0.25	9.2 ± 0.12	0.5 ± 0.05	4.25

Table 5 K_P for all materials as determined from GRG fits to the size reduction data, average value over all humidities and the value at 40% RH as used in the calculations.

	Materials	Average K_p, [1/s]	K_p S.D.	K_p at 44%Rh, [1/s]	Milling time range for determining K_p
Amorphous	Fused Silica	0.184	0.0061	0.212	0s-to end
	Lithium silicate	0.134	0.0391	0.150	0s-to end
	Sodium aluminium silicate	0.191	0.0158	0.195	0s-to end
Crystalline	Quartzite	0.132	0.014	0.11	17s-to end (180s)
	Lithium silicate	0.013	0.004	0.013	140s-to end (340s)
	Sodium aluminium silicate	0.2	0.014	0.13	4s-to end (~180s)
Crystalline (bulk)	Quartzite (Bulk)	0.194	0.0137	0.191	0-17s
	Lithium silicate (Bulk)	0.022	0.028	0.021	0-140s
	Sodium aluminium silicate (Bulk)	0.437	0.024	0.437	0-4s

Table 6 Summary of mechanical and milling characterisation.

Amorphous

Materials	Hardness, GPa	K_c, MPa.m$^{0.5}$	H/K_c^2, m^2/kJ	K_p @44%, 1/s
Fused silica	6.64	1.91	1.82	0.18
Sodium aluminium silicate	7.22	1.3	4.27	0.195
Lithium silicate	8.56	0.64	20.90	0.21

Inter-crystallite

Quartzite	1.37	0.69	2.88	0.191
Sodium aluminium silicate	1.24	0.54	4.25	0.437
Lithium silicate	1.15	1.02	1.11	0.021

Crystallite

Quartzite	8.16	1.16	6.06	0.11
Sodium aluminium silicate	5.44	0.74	9.93	0.13
Lithium silicate	1.15	1.02	1.11	0.013

Appendixes

Table A-1: XRD data of three crystalline materials.

Features	Sample 1	Sample 2	Sample 3
Compound name	Silicon Oxide	Lithium Silicate	Sodium Aluminium Silicate
Common name	α-Si O_2	-	Carnegieite
Molecular formula	SiO_2	$Li_2Si_2O_5$	$NaAl(SiO_4)$
Crystal system	Hexagonal	Orthorhombic	Orthorhombic
Space group	P3221	Ccc2	Pb21a
Space group number	154	37	29
a	4.8915	5.8070	10.2610
b	4.8915	14.5820	14.0300
c	5.3885	4.7730	5.1566
α	90	90	90
β	90	90	90
γ	120	90	90
Cell volume (10^6 pm^3)	111.66	404.14	742.35
Z	3	4	8
RIR	3.02	1.84	1.13

Table A-2: Materials parameters of materials used in the simulations.

	Stainless steel ball and capsule	Fused silica	Quartzite
Density (kg/m^3)	7800	2190	2780
Young's modulus (GPa)	190	83.1	12.72
Poisson's ratio	0.34	0.33	0.33

Influence of Mechanical Properties on Milling of Amorphous and Crystalline Silica-Based Solids
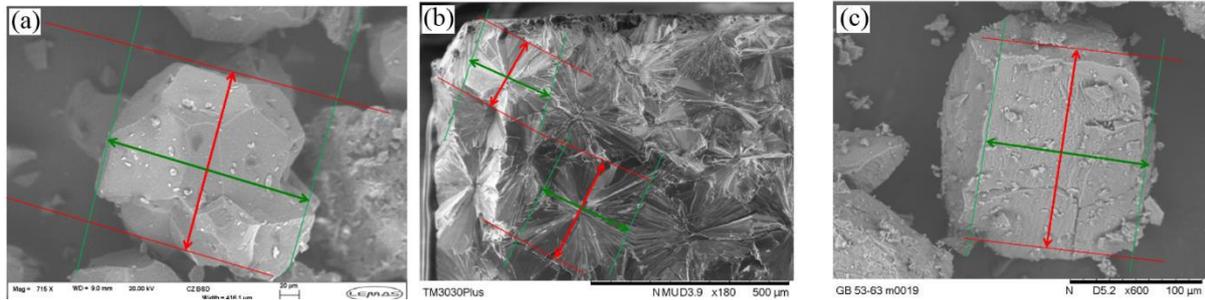
Figure 1: The Ferret's diameter measurement from SEM images: (a) quartzite, (b) lithium silicate and (c) sodium aluminium silicate.

Figure 2: The nano-indentation loading-unloading curves on fused silica (left), amorphous lithium silicate (middle) and amorphous sodium aluminium silicate (right). For illustrative purposes the starting displacements of the amorphous lithium and sodium alumina silicate are shifted to the right by 1.5 and 2.5 μm, respectively.
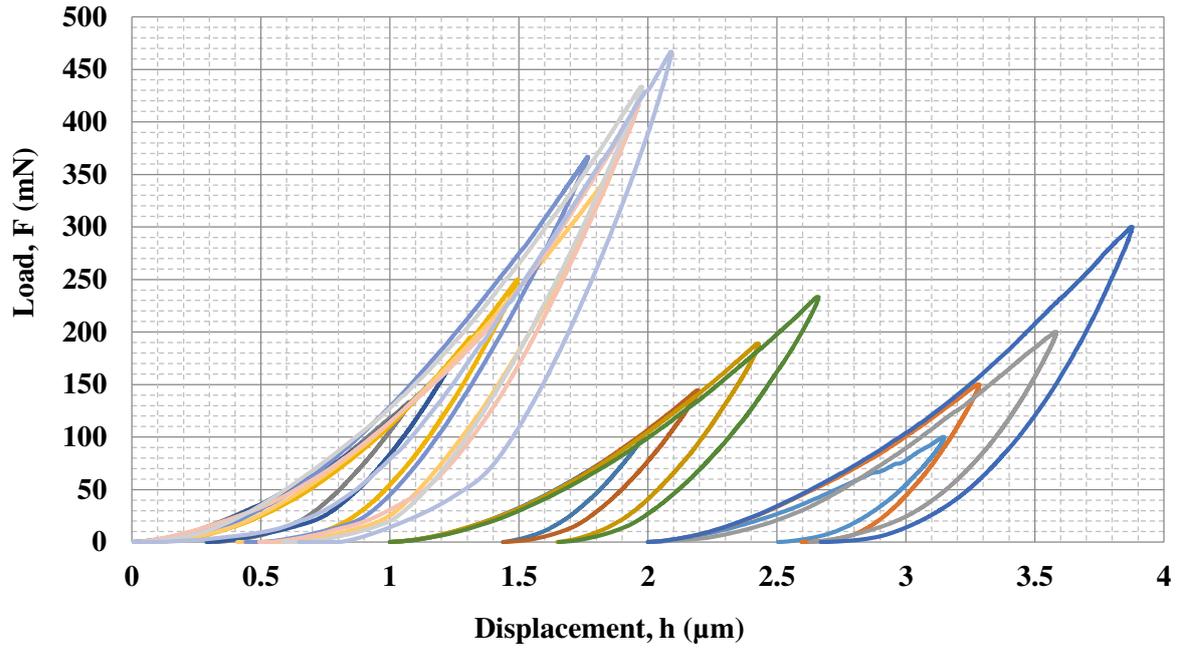
Figure 3: The nano-indentation loading-unloading curves on quartzite (left), crystalline lithium silicate (middle) and crystalline sodium aluminium silicate (right). For illustrative purposes the starting displacements of the lithium and sodium alumina silicates are shifted to the right by 1 and 2 μm, respectively.

Figure 4: Vickers indent at 1.5 N load on sodium aluminium silicate with diagram of the half length of the diagonal indent (a) and diagram of crack length (b).
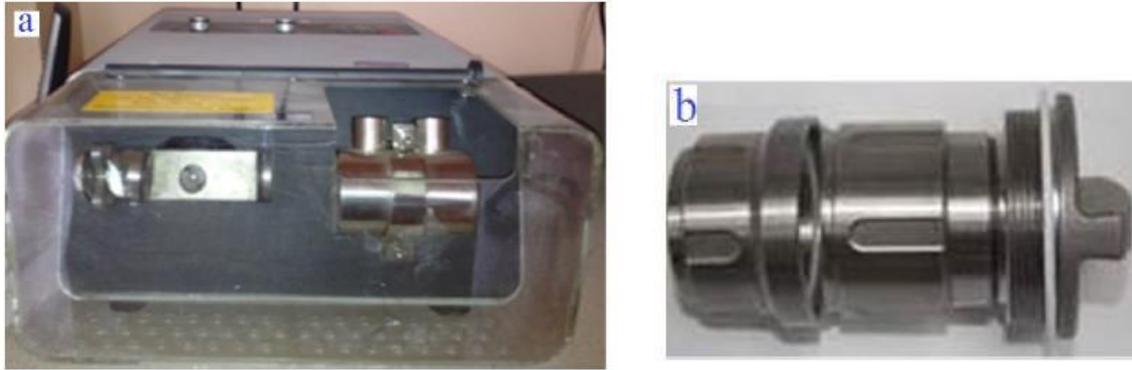
Figure 5: Milling equipment: (a) the Retsch MM 200 single ball mill (b) the stainless steel grinding capsule.
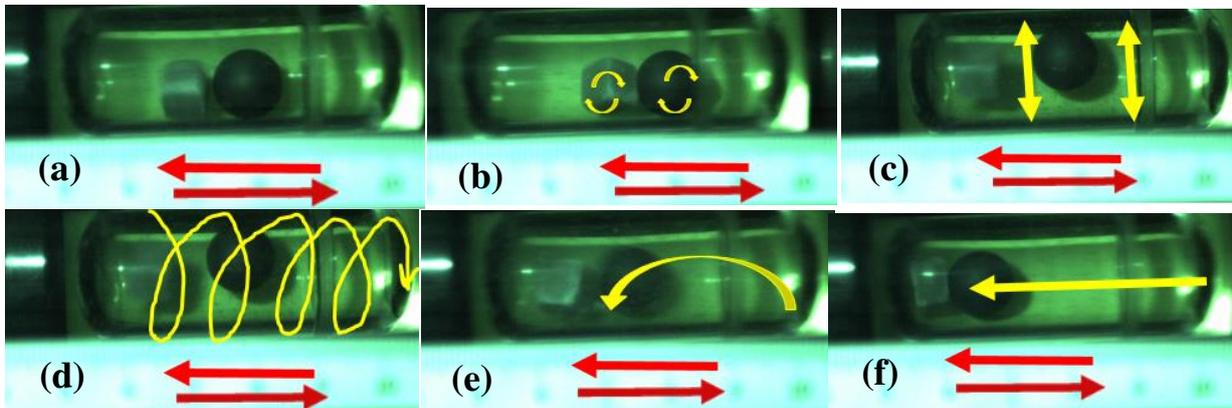
Figure 6: Movement of 12 mm grinding media and cube sample at 30 Hz; (a) static pattern; (b) short swirling; (c) vertical movement; (d) long swirling; (e) roll impacting; (f) fly impacting.

Figure 7: Size reduction ratio of amorphous (a-c) and crystalline specimens (d-f) as a function of grinding time at 30 Hz for each six materials at 4 different relative humidities from 5 to 74%RH; (a) fused silica; (b) lithium silicate; (c) sodium aluminium silicate; (d) quartzite; (e) lithium silicate; (f) sodium aluminium silicate.
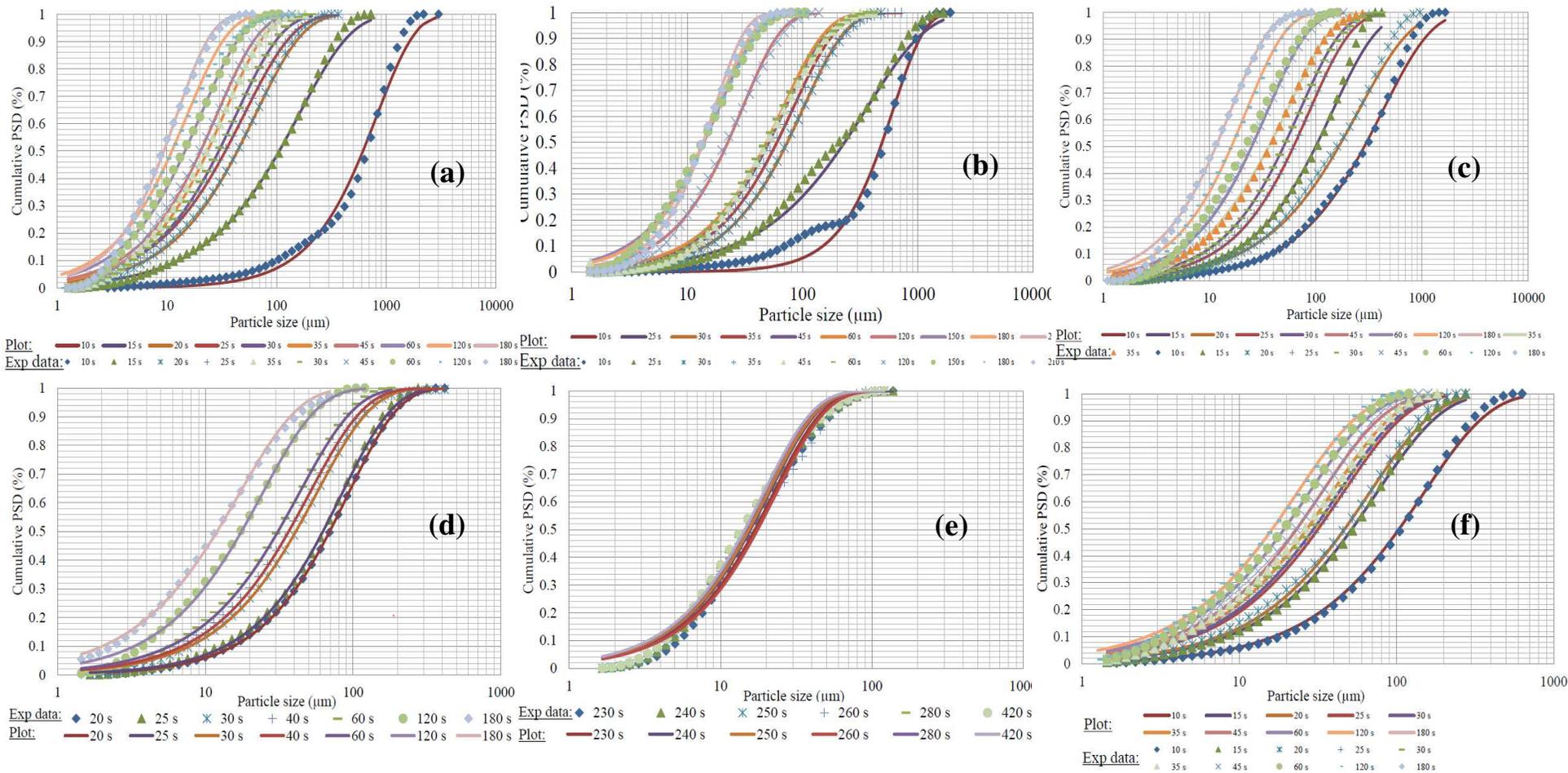
Figure 8: The fitted cumulative Rosin-Rammler distribution model compared with the experimental data of amorphous (a-c) and crystalline specimens (d-f) for various grinding times for; (a) fused silica; (b) lithium silicate; (c) sodium aluminium silicate; (d) quartzite; (e) lithium silicate; (f) sodium aluminium silicate.
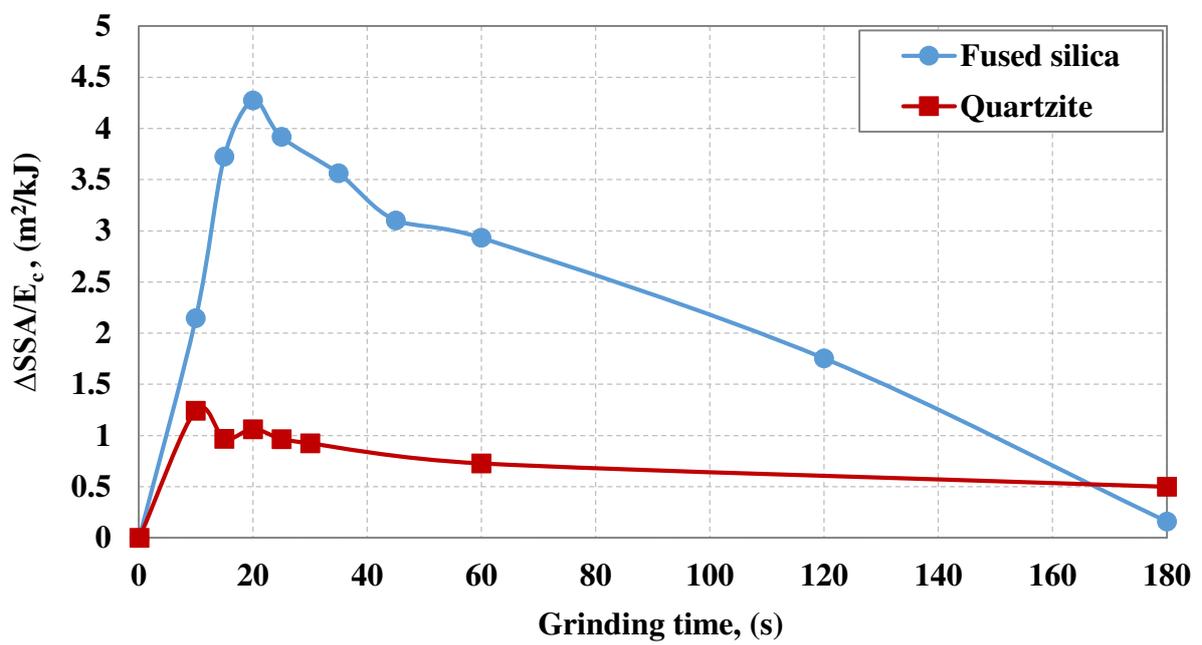
Figure 9: Energy utilisation of fused silica and quartzite as a function of grinding time.
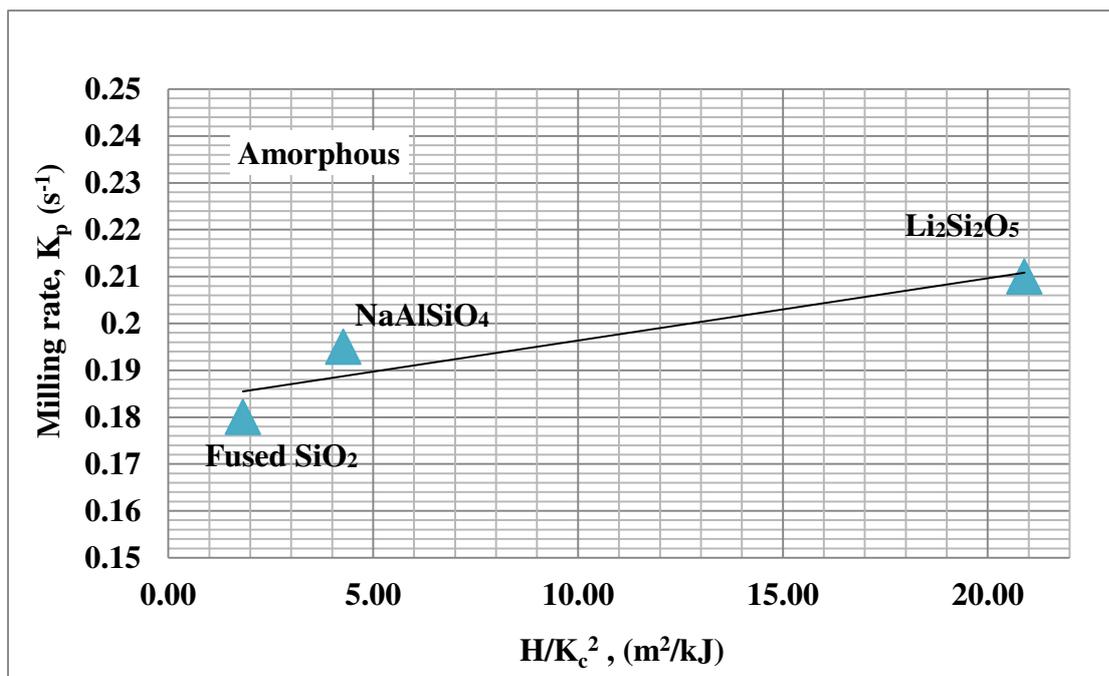
Figure 10: The milling rate constant as a function of breakability index for amorphous

silicate materials.

Figure 11: Milling rate constant for bulk crystalline specimens, representing inter-crystallite fracture along grain boundaries as a function of the breakability index for crystalline silicate materials.
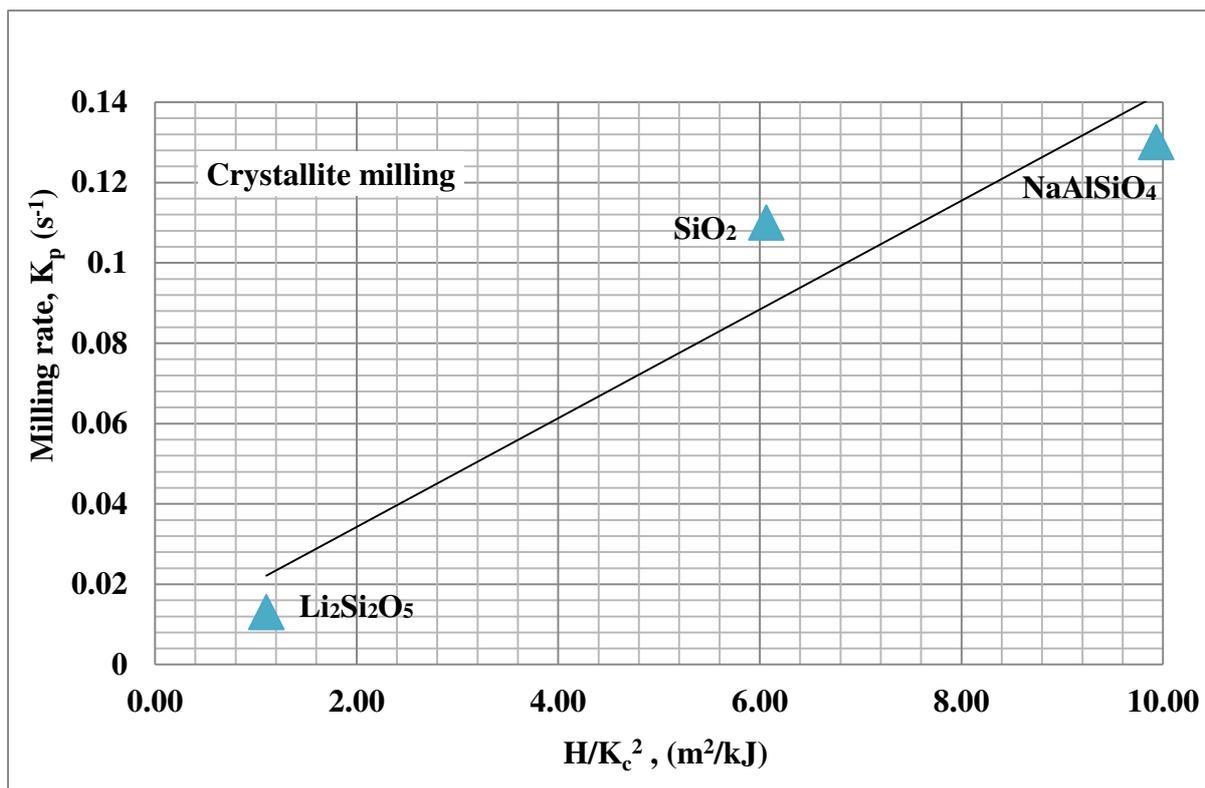
Figure 12: Milling rate constant for crystallite milling as a function of breakability index.

Figure 13 SEM micrographs of lithium silicate showing the crystallite and a crack generated from outside the crystallite and going through it and out again.

Figure A-1: Contact angle measurement for (a) amorphous fused silica; (b) amorphous lithium silicate; (c) amorphous sodium aluminium silicate; (d) crystalline quartzite; (e) crystalline lithium silicate; (f) crystalline sodium aluminium silicate

Figure A-2: SEM images of milled fused silica; (a) breakage and fatigue on mother particle; (b) chipped particles from mother particles; (c) coarse particles; and (d) milled sample at 180 s

Figure A-3: SEM images of milled amorphous lithium silicate; (a) breakage on mother particles; (b) chipped particles from mother particles; (c) coarse particles; (d) milled sample at 180 s.
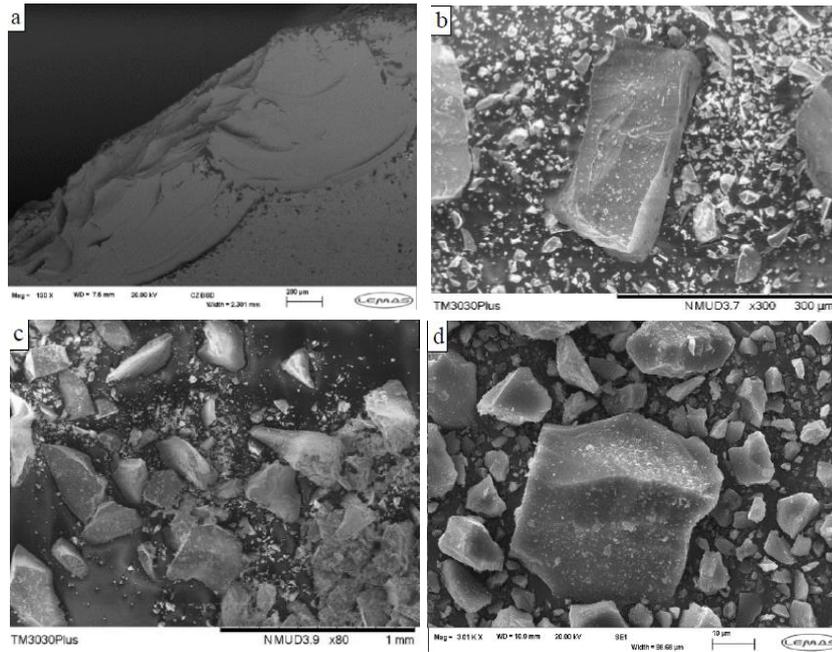
Figure A-4: SEM images of milled amorphous sodium aluminium; (a) breakage on mother particles; (b) chipped particles from mother particles; (c) coarse particles; (d) milled sample at 180 s.
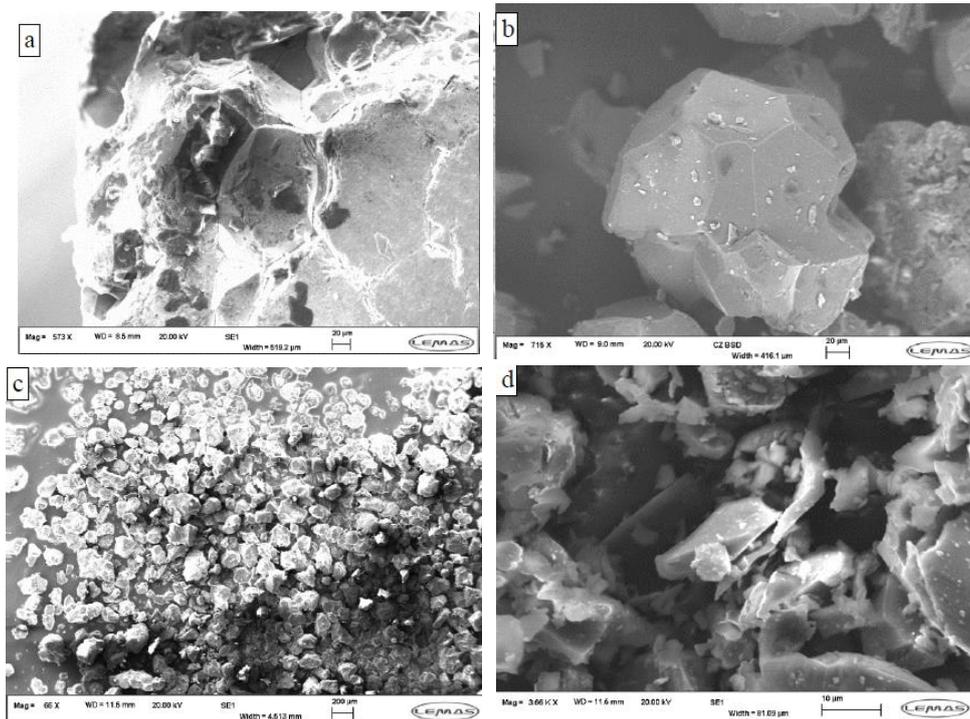

Figure A-5: SEM images of crystalline quartzite; (a) corner and edge damage, at grinding time of 2 s; (b) chipped hexagonal quartzite grains; (c) the liberated quartz grains; and (d) grinding limit size of quartzite.
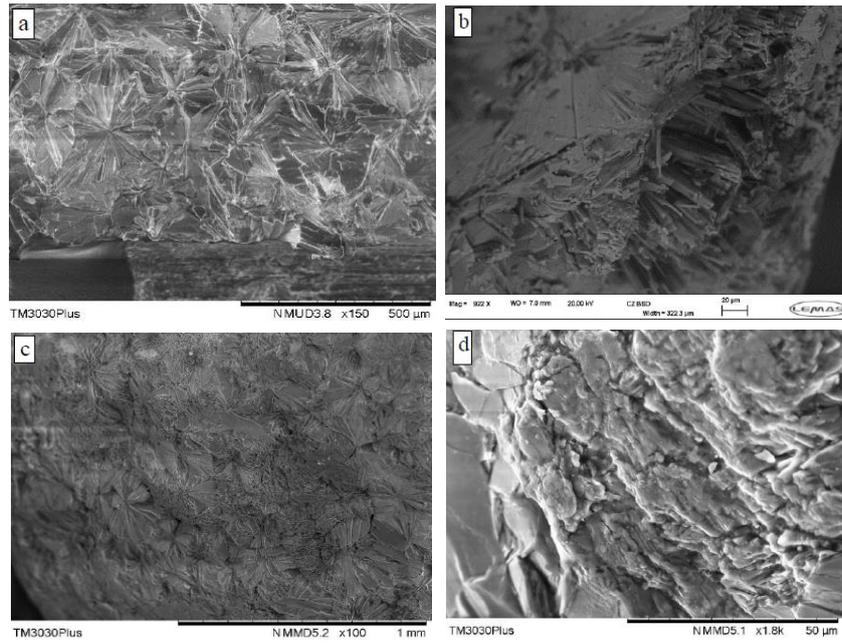
Figure A-6: SEM images of crystalline lithium silicate; (a) fresh origanl surface; (b) corner of mother particle after chipping at grinding time of 1 s; (c) and (d) the crushed mother particle surface.
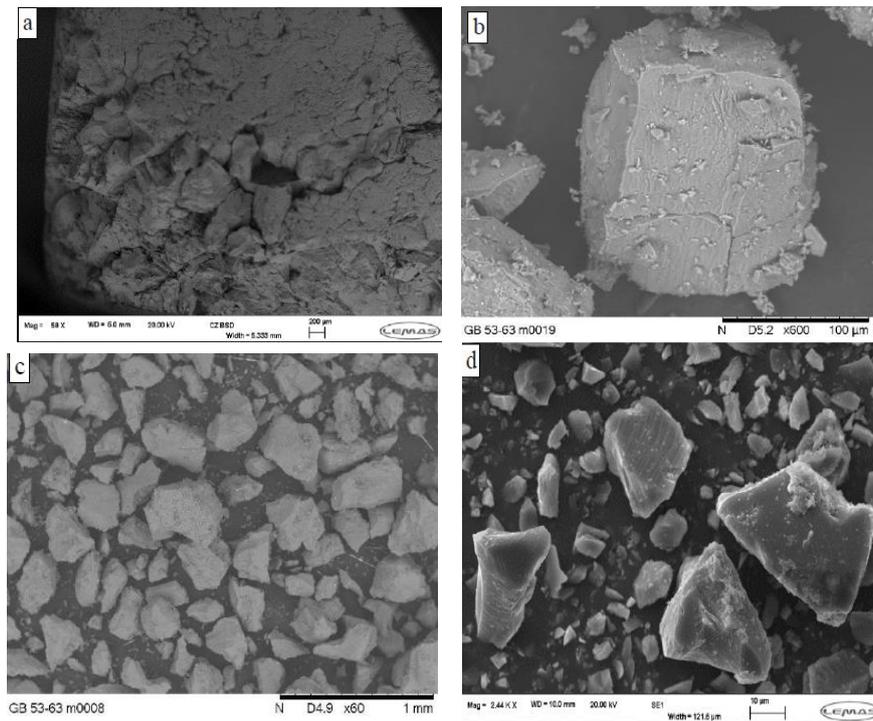

Figure A-7: SEM images of crystalline sodium aluminium silicate; (a) corner of mother particle at 1 s; (b) chipped grain particle; (c) the liberated quartz grains; and (d) grinding limit size.